

PAPER • OPEN ACCESS

Discrimination of simple objects decoded from the output of retinal ganglion cells upon sinusoidal electrical stimulation

To cite this article: Andrea Corna *et al* 2021 *J. Neural Eng.* **18** 046086

View the [article online](#) for updates and enhancements.

You may also like

- [Progress in electron- and ion-interferometry](#)
Franz Hasselbach
- [Short-range organization and photophysical properties of CdSe quantum dots coupled with aryleneethynylenes](#)
Christoph P Theurer, Antonia Weber, Martin Richter et al.
- [Tickling the retina: integration of subthreshold electrical pulses can activate retinal neurons](#)
S Sekhar, A Jalligampala, E Zrenner et al.



PAPER

OPEN ACCESS

RECEIVED
4 February 2021

REVISED
26 May 2021

ACCEPTED FOR PUBLICATION
28 May 2021

PUBLISHED
17 June 2021

Original content from
this work may be used
under the terms of the
[Creative Commons
Attribution 4.0 licence](#).

Any further distribution
of this work must
maintain attribution to
the author(s) and the title
of the work, journal
citation and DOI.



Discrimination of simple objects decoded from the output of retinal ganglion cells upon sinusoidal electrical stimulation

Andrea Corna^{1,2,3,7} , Poornima Ramesh^{4,5}, Florian Jetter^{1,3}, Meng-Jung Lee^{1,3}, Jakob H Macke^{4,5,6} and Günther Zeck^{1,7,*}

¹ Neurophysics, NMI Natural and Medical Sciences Institute at the University Tübingen, Reutlingen, Germany

² Institute for Ophthalmic Research, University of Tübingen, Tübingen, Germany

³ Graduate School of Neural Information Processing/International Max Planck Research School, Tübingen, Germany

⁴ Computational Neuroengineering, Technical University München, München, Germany

⁵ Machine Learning in Science, University of Tübingen, Tübingen, Germany

⁶ MPI for Intelligent Systems, Tübingen, Germany

⁷ Biomedical Electronics and Systems, EMCE Institute, TU Wien, Wien, Austria

* Author to whom any correspondence should be addressed.

E-mail: guenther.zeck@tuwien.ac.at

Keywords: electrical stimulation, retina prosthetics, CMOS-based microelectrode array, rd10 mouse retina, non-human primate retina

Supplementary material for this article is available [online](#)

Abstract

Objective. Most neuroprosthetic implants employ pulsatile square-wave electrical stimuli, which are significantly different from physiological inter-neuronal communication. In case of retinal neuroprosthetics, which use a certain type of pulsatile stimuli, reliable object and contrast discrimination by implanted blind patients remained challenging. Here we investigated to what extent simple objects can be discriminated from the output of retinal ganglion cells (RGCs) upon sinusoidal stimulation. **Approach.** Spatially confined objects were formed by different combinations of 1024 stimulating microelectrodes. The RGC activity in the *ex vivo* retina of photoreceptor-degenerated mouse, of healthy mouse or of primate was recorded simultaneously using an interleaved recording microelectrode array implemented in a CMOS-based chip. **Main results.** We report that application of sinusoidal electrical stimuli (40 Hz) in epiretinal configuration instantaneously and reliably modulates the RGC activity in spatially confined areas at low stimulation threshold charge densities (40 nC mm⁻²). Classification of overlapping but spatially displaced objects (1° separation) was achieved by distinct spiking activity of selected RGCs. A classifier (regularized logistic regression) discriminated spatially displaced objects (size: 5.5° or 3.5°) with high accuracy (90% or 62%). Stimulation with low artificial contrast (10%) encoded by different stimulus amplitudes generated RGC activity, which was classified with an accuracy of 80% for large objects (5.5°). **Significance.** We conclude that time-continuous smooth-wave stimulation provides robust, localized neuronal activation in photoreceptor-degenerated retina, which may enable future artificial vision at high temporal, spatial and contrast resolution.

1. Introduction

Avoidance of obstacles or discrimination of nearby objects represents one of the major needs of blind patients. Object discrimination and recognition tasks are routinely performed after blind patients receive a prosthetic implant [1]. Although in several cases remarkable results were obtained, in the best cases achieving reading acuity (for retinitis pigmentosa

patients: [2], for age-related macular degeneration, AMD, patients: [3], statistical evaluation of vision restoration provides a mixed picture. Major challenges remain, including fading of evoked precepts [4, 5], low spatial resolution which does not overcome legal blindness [6] and a reduced contrast perception [7].

To improve temporal, spatial and contrast resolution two main strategies need to be pursued. The first is improving electrode design. The second is

optimizing pulsatile stimulation or finding an alternative to it. To improve spatial resolution, 3D electrodes and localized return electrodes, which confine the electric field during stimulation, have been suggested recently [8–11]. However, improving electrodes is not sufficient if axons of passage are within the activation range. One promising approach suggests the use of ultra-short stimuli (<0.1 ms), which achieve selective activation of ganglion cells in rabbit [12] and primate retina [13] but require the precise knowledge of the axon's path [14–16]. Contrast resolution achieved by state-of-the-art implants and pulsatile stimuli (1 and 2 ms) in blind patients were limited to few grey levels [7, 17]. Therefore, recent approaches, aimed to overcome square-wave pulses, inferred the mean effective stimulus from spike-triggered averaging white-noise current input [18, 19] but obtained very short, almost pulsatile waveforms. Another alternative is sinusoidal stimulation at relatively low frequencies (10–50 Hz). With such stimuli, a more confined retinal activation was shown as compared to short pulses [20] as well as reliable activation estimated at single cell level [15]. However, a quantitative evaluation of continuous sinusoidal stimulation to study the level of spatial and contrast resolution obtained from the readout of a large population (~ 1000) of retinal ganglion cells (RGCs) is missing.

Evaluation of different stimulation strategies at single spike resolution in large neuronal populations has not been demonstrated, mainly because of the artefact evoked by electrical stimuli. Recording of large populations of RGCs was shown by Ho *et al* in subretinal configuration using a combination of two micro-electrode arrays [21] but with blanking several milliseconds following each stimulus pulse. In epiretinal configuration single-cell resolved recording and axon tracking has been achieved for sub-millisecond pulsatile stimuli [14].

Here we report on the spatial and temporal performance achieved with sinusoidal stimuli in *ex vivo* retina mainly of the adult photoreceptor-degenerated mouse. Control experiments were performed on the retinae of healthy mice and non-human primates. The experiments made use of a high-density complementary metal oxide semiconductor (CMOS)-based microelectrode array (MEA) [22], which comprises a dense stimulation electrode array and a second, interleaved recording array. By simultaneously stimulating and electrically imaging up to hundreds identified RGCs within one experiment, we tested the efficiency of epiretinal stimulation in terms of reliability, charge threshold and long-term stability. We addressed the problem of quantifying spatial resolution and artificial contrast discrimination, at the population level using a logistic regression (LR) model. Our data show, to our knowledge, for the first time, that in photoreceptor-degenerated retina electrically stimulated objects separated by $32\text{ }\mu\text{m}$, and

contrast levels of 10%, can be classified with high fidelity.

2. Methods

2.1. Preparation of the retina and extracellular recording using CMOS based MEA

Retina preparation was performed using adult B6.CXB1-Pde6brd10/J (retinal degeneration 10 (rd10)) and C57BL/6J (wild-type (WT)) mice of either sex as described previously [18, 23]. Results are reported here from retinae obtained from a total of eight rd10 mice and four WT mice. With the exception of one rd10 mouse (postnatal day 80, figure 2) all other animals are aged between 130 and 260 d; a late degeneration stage [24]. The age of the adult WT mice ranged between postnatal-day 59 and 270. We also report on data obtained from two different non-human primates obtained from terminally anesthetized macaque monkeys (*Macaca mulatta* and *Macaca fascicularis*; age 8–10 years), used by another laboratory in the course of their experiments. All experimental protocols were approved by the Regierungspräsidium Tübingen according to German federal laws on animal welfare.

Immediately after enucleation, the anterior portion of the eye and the vitreous were removed. From the posterior portion of the eye segments of peripheral retina that were well attached to the pigment epithelium were dissected, isolated from the pigment epithelium, and placed, RGC side down, on the planar MEA. Retina samples were kept in dark during the length of the recording, recordings were performed after 30–45 min of dark adaptation. All experimental protocols were reported and approved by the local authorities according to German federal laws on animal welfare.

Prior to the experiment, the surface of the CMOS MEA was gently cleaned with detergent (Tickopur R60, 5%, Stamm/Berlin, 80 °C), rinsed with bi-distilled water and treated for 30 s with a plasma cleaner (Harrick Plasma). The hydrophilic chip surface was coated with $\sim 500\text{ }\mu\text{l}$ (1 mg ml^{-1}) poly-L-lysine (P1399, MW 150–300 kDa, Sigma, Germany) to facilitate adhesion of the retina. Retinal portions ($\sim 4\text{ mm}^2$) were transferred to the chip chamber and placed with RGCs in close contact with the electrodes (figure 1(C)). The CMOS MEAs were rinsed prior to positioning of the retina and continuously perfused (flow rate $2\text{--}4\text{ ml min}^{-1}$ and temperature $34\text{ }^{\circ}\text{C}$ – $36\text{ }^{\circ}\text{C}$) with carbogenated Ames medium (A1420, Sigma). The chip comprising the attached retina was mounted on the amplifier placed on a motorized x and y stage (CONEX CC, Newport) in an upright microscope (BX 51W, Olympus).

To evaluate the effects of network activity on evoked response, we performed control experiment using $100\text{ }\mu\text{M}$ DNQX (Tocris Cat. no. 2312) and

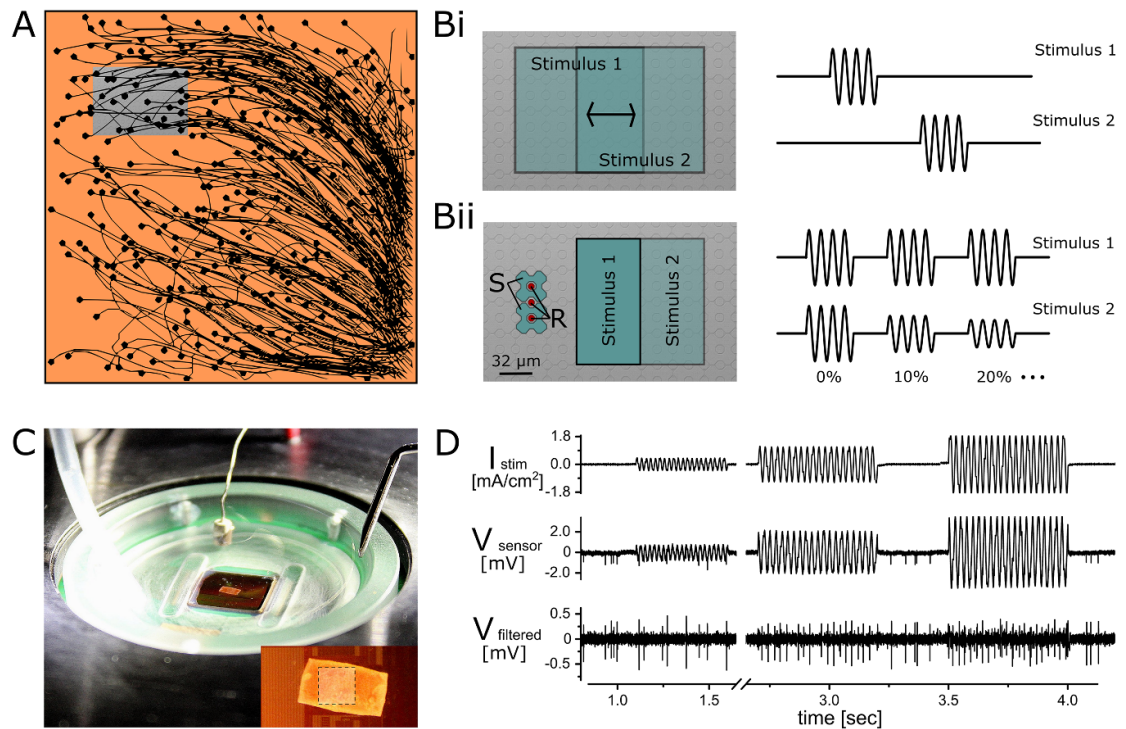


Figure 1. Bidirectional interfacing of *ex vivo* retina with CMOS MEA and description of discrimination tasks. (A) Electrical imaging of *ex vivo* retina using CMOS MEA shows the identified positions for the RGC somas (circle) and axons (line) within the $1 \times 1 \text{ mm}^2$ sensor array area. Details of the grey area are shown in (B). (B) Schematic of the spatial (Bi) and contrast (Bii) discrimination task. Scanning electron microscopy images (grey) show details of the CMOS MEA array with stimulation (S) and recording (R) electrodes. For electrode dimensions see the section 2. (Bi) Spatial discrimination task: two partially overlapping stimulation areas, stimulus 1 and 2, are selected and stimulated alternating with the same stimulation strength for 50 repetitions. In the discrimination task the RGC population response is assigned either to stimulus 1 or to stimulus 2. (Bii) Contrast discrimination task: two adjacent stimulation areas, stimulus 1 and 2, are selected and activated simultaneously with different stimulation strength to create a single contrast level for 40 repetitions. The contrast discrimination task consists of response discrimination between different contrast levels. (C) Experimental setup showing the CMOS MEA with interfaced retina in a culture chamber, perfused by a heated inlet. In addition, the outlet of the perfusion system and the Ag/AgCl reference electrode are visible. The insert shows the interfaced *ex vivo* retina and the electrode array (1 mm^2 , dashed outline). (D) Top: sinusoidal stimulation current density for three different amplitudes and 40 Hz frequency. Middle: raw recording from one of the 4225 recording electrodes, with stimulation artefact. Bottom: signal after filtering/artefact removal, demonstrating spontaneous and stimulus-induced spikes.

20 μM AP5 (Tocris Cat. no. 3693) in addition to the standard Ames medium in order to block glutamatergic synaptic inputs to RGCs. Recordings were performed after 30 min of continuous perfusion to guarantee the complete application of the drug.

A CMOS-MEA comprising 4225 recording electrodes, with an electrode pitch of 16 μm (65×65 lattice and total area: $1 \times 1 \text{ mm}^2$) and 1024 stimulation electrodes (electrode area: $632 \mu\text{m}^2$) was used (figures 1(B) and (C)) (CMOS-MEA5000-System, Multi Channel Systems MCS GmbH). Recordings were performed at 20 kHz using CMOS-MEA Control software (Multi Channel Systems MCS GmbH). Signal was band-pass filtered at 1–3.5 kHz to remove artefacts of electrical stimulation. In some cases, a larger band for the filter was used (300–4000 Hz) in combination with an artefact reduction method (offset correction and baseline subtraction) (figure 1(D)). Spike sorting was performed to detect single cell firing, using the implementation of an ICA-based algorithm [25] in the CMOS-MEA-Tools software

(Multi Channel Systems MCS GmbH). This software allows tracking of the axons using average electrical images obtained by a spike triggered averaging (STA) of the recorded extracellular voltages on all 4225 electrodes (figure 1(A)). In detail, the axon path is identified as follows: The start point is identical to the sensor position associated with the RGC after spike sorting. At this position the maximum absolute amplitude of the RGC spike is recorded. Sensors associated to the axon are identified based on threshold crossings in the mean electrical images computed for the entire sensor array. The averaging procedure reduces the noise of individual electrical images, obtained for individual spikes. Because of the stereotyped action potential generation and propagation, extracellular signals along the axon path are detected as threshold crossings. The threshold is calculated for each sensor individually as $5 \times$ the standard deviation of the STA voltage in the time interval of 10 ms before the spike peak amplitude. Typical electrical images have been published previously [26].

2.2. Electrical stimulation using CMOS-based MEA

We applied sinusoidal stimuli of two different frequencies (25 and 40 Hz) and of different amplitudes with different electrode size areas using selected electrodes of the CMOS-MEA. Applying voltages to the stimulation electrodes evokes capacitive currents in the electrolyte and the retina above the electrode. The stimulation current density is proportional to the time derivative of the electrode voltage and scales with the specific electrode capacitance c : $i_{\text{stim}} = c \times dV/dt$. For sufficiently large stimulation currents, a high specific capacitance is required. So-called high K oxides provide a specific capacitance of 1 and 2 $\mu\text{F cm}^{-2}$, depending on the oxide thickness and material, with a stimulation amplitude up to 3 V [22, 27]. However, to increase the specific capacitance we omitted here the last dielectric layer and relied on the native oxide of the top titanium nitride electrode.

The stimulation current (figure 1(D)) was measured as follows. An Ag/AgCl pellet (E201ML, Science Products) was used as a counter electrode and located in the electrolyte above the CMOS MEA. The stimulation current was calculated from the voltage drop across a serial 10 Ω resistor in series with the Ag/AgCl electrode. The voltage drop was amplified using a commercial voltage amplifier (DLPVA, Femto Messtechnik GmbH, Berlin, Germany) and recorded using the analog channel of the interface board of the CMOS MEA 5000. Stimulation charge and charge density was calculated during the anodic stimulation phase. The specific capacitance of our electrodes was 5.5 $\mu\text{F cm}^{-2}$ (supplementary figure 1 (available online at stacks.iop.org/JNE/18/046086/mmedia)). The total stimulation charge during a full sinusoidal stimulation period was zero.

For both, the spatial and contrast discrimination tasks, the retina was stimulated for 100 ms with a 40 Hz sinusoidal stimulus with 500 ms breaks between stimuli (figure 1(B)). For spatial discrimination, two stimuli were alternated between each other 50 times. In the contrast discrimination task, for one contrast level, stimulation was applied at different intensities from two adjacent stimulation areas. The difference of current intensity between the two areas defined the artificial contrast by the equation: artificial contrast = (intensity 1 – intensity 2)/(intensity 1 + intensity 2). Each contrast level was repeated 40 times.

2.3. Analysis

Data analysis was performed using custom analysis code written in Python. Distance of the cell from the stimulation area was calculated from the center of the electrode stimulation area. Reliability was calculated evaluating the response of a cell to sinusoidal cycles and defined as follows: a cell was identified as responding to a cycle, when firing at least once during the cycle. A cell responding to every cycle will have

reliability of 1. The total reliability of a cell during a recording/stimulation protocol is calculated as the mean reliability of single repetitions. To take in to account spontaneous activity, we also evaluated the relative cell response as: cell response = (spikes during stimulation – spikes during spontaneous activity)/(spikes during stimulation + spikes during spontaneous activity).

Evaluation of the activation radius was obtained by fitting a one-dimensional Gaussian distribution to the cell response versus the distance of the cell from the electrode center. For the evaluation of cell responses in the spatial jitter task, a symmetrical two-dimensional Gaussian was used.

2.4. LR model

2.4.1. LR model

To check whether RGC responses reliably reflected differences in stimuli for the spatial and contrast discrimination tasks, we used a LR model [28]. LR describes the probability of one of two possible events (denoted by $y = 0$ or $y = 1$), given some factors x . For example, with the spatial discrimination task, we would use the LR model to predict whether the stimulus was at the first position ($y = 0$) or at the second position ($y = 1$), given the RGC responses x , under the LR model, we write down the probability of the stimulus-identity $p(y|x)$ as follows:

$$z = w \cdot x + b$$

$$r = \frac{e^{-z}}{1 + e^{-z}}$$

$$p(y|x) = r^y (1 - r)^{1-y},$$

where w is a vector of regression parameters, b is a bias parameter, and x a vector consisting of the spike count for each neuron. The activation variable z (the vector product of w and x) is passed through a sigmoid function to obtain the model-predicted probability r of the stimulus having identity 1. The values of w correspond to the strength of contribution of each neuron in decoding the stimulus identity i.e. how strongly each neuron's response influences $p(y|x)$. We can learn these w of the LR model by maximizing an objective function: the log probability $\log p(y|x)$ with respect to w , for the set of responses x obtained experimentally and the corresponding stimulus identity y :

$$w^* = \operatorname{argmax}_w \frac{1}{2N} \sum_{i=1}^N y_i \log r_i + (1 - y_i) \log (1 - r_i)$$

where N is the number of times the experiment was repeated. The objective function was maximised to find w using the scipy optimization package [29].

For the spatial discrimination task, we showed $N = 50$ repetitions of two alternating stimuli at different positions on the stimulation grid. We denoted

position 1 as $y = 0$ and position 2 as $y = 1$. For each stimulus and repeat, we constructed x by counting the total number of spikes fired by each recorded neuron between stimulus onset and offset i.e. in each 100 ms window while the stimulus was presented, resulting in $2N = 100$ vectors x , each of which had a length equal to the number of neurons recorded. We then trained the LR model on x and the corresponding y values, by computing the log probability $\log p(y|x)$ and maximizing it with respect to the parameters w .

For the contrast discrimination task, we showed $N = 40$ repetitions of stimuli of seven different contrast levels. The contrast levels were 0%, 10%, 20%, 30%, 40%, 50% and 100%. We defined six different LR models—in each model, the 1st stimulus ($y = 0$) was always the 0% contrast, while the 2nd stimulus ($y = 1$) varied from 10% to 100%—in other words, the discrimination task always involved differentiating a non-zero contrast stimulus from the zero-contrast stimulus. As with the spatial discrimination task, for each of the seven stimuli and each repeat, we constructed response vectors x by counting spikes fired by all recorded neurons during stimulus presentation. We thus had 280 different response vectors, and 80 per LR model. Once again, we trained the six LR models on the corresponding x, y pairs by maximizing the log probability of y given x .

While training the LR models, we performed a random 80–20 split of the data repetitions into a training set and a test set. The training data was used to learn the regression parameters w . The test dataset, which the model did not have access to during training, was used to calculate the prediction accuracy of the model. The random split was repeated five times; the models were fit anew for each split and the results were averaged across these five splits.

2.5. Regularization and cross-validation

In order to prevent the regression weights w from varying too much from neuron to neuron, we imposed a smoothing L2 penalty [30] i.e. we modified the objective function to include the squared norm of w i.e. $\lambda|w|^2$, and maximized this new objective function with respect to w . The hyperparameter λ controlled the strength of the smoothing penalty.

We optimized λ by performing a grid search with five-fold cross-validation. We first defined a grid of 30 λ values ranging from 0.1 to 100 at uniform intervals in log-space. For each value of λ , we randomly split the repetitions in the data into five folds, where each fold contained 80% of the repetitions as the training set and 20% as validation set (note that this five-fold splitting occurred on the training data input to the model, i.e. 80% of all available experimental data). With this value of λ from the grid, we cycled through the five folds, fit the model on the training set and computed the objective function on the validation set. This cross-validated objective function was averaged across the five folds. The λ with the

highest value of the cross-validated objective function was chosen, and used for all further analysis with the model.

2.5.1. Accuracy score

We calculated the predictive accuracy of the trained models for both discrimination tasks on the test data (20% of all experimental data). The accuracy score is defined as follows:

$$\text{accuracy} = \frac{p(\hat{y} = 1|y = 1) + p(\hat{y} = 0|y = 0)}{p(y = 1) + p(y = 0)},$$

where \hat{y} is the model prediction. In practice, this score is calculated as: $\frac{\text{number of correct model predictions}}{\text{total number of model predictions}}$.

Thus, this value is bounded between 0 and 1. An accuracy score of 1 indicates that the model perfectly predicts the stimulus identity given responses. A score below 0.5 indicates that the model cannot decode stimulus identity from the responses, and that simply guessing the stimulus identity at random would give us better performance than the model.

2.5.2. Accuracy with a reduced neural population

We next wanted to check how robust the decoding performance was i.e. how many neurons from the population were actually required to get maximal test accuracy. In order to do this, we repeated the analysis described above, but using responses only from a fraction of the neural population recorded. We first sorted the neurons in descending order of their absolute value in regression parameter w . Note that this value indicates the contribution of a particular neuron's responses to the decoding performance in the training data for the LR model. We then used the responses of only a fraction of the neurons with the highest regression values to fit new LR models, and calculated the test accuracy of these models. The population fractions used were 1%, 10%, 20%, 40%, 50% and 75%.

3. Results

Here we propose and demonstrate an efficient strategy of discriminating spatial and contrast differences of simple objects using the stimulated retinal activity. We base our approach on the following three hypotheses: (a) retinal cells or networks in photoreceptor degenerated retinas are modulated reliably (without fading) by continuous sinusoidal electrical stimuli; (b) the modulation of the spiking of retinal neurons decreases strongly with distance from the stimulating electrode and (c) the readout of ganglion cells subpopulations from different stimuli enables discrimination of spatial displacement and contrast. Results supporting these hypotheses and how they are combined into an efficient decoding scheme are presented in this section.

A prerequisite in the development and evaluation of any stimulation strategy is the simultaneous

recording of the evoked activity, ideally without stimulation artefacts [31]. Here we took advantage of a CMOS-based MEA [22] with spatially interleaved 1024 stimulation electrodes (stimulation electrode pitch: 32 μm , electrode area: 632 μm^2 ; equivalent diameter: 28.3 μm) and 4225 electrodes (figure 1).

Application of sinusoidal stimuli to the selected electrodes modulates the interfaced retinal network (figure 1(D)) and leads to rhythmic ganglion cell activity. To identify the appropriate ‘stimulation range’ of the interfaced retina different stimulation amplitudes were applied (figure 1(D)). Typical stimulation currents applied by the CMOS MEA range between 1 and 6 μA (see section 2). Notably, because of the low capacitance (35 pF) of a single stimulation electrode (632 μm^2) the stimulation current does not change if retina is interfaced to the electrode array or not (supplementary figure 1), in contrast to the majority of electrical stimulation approaches [32, 33]. The electrical characterization of the capacitive electrodes (frequency behavior, linearity with stimulus amplitude and with stimulation area) is presented in the supplement (supplementary figure 1).

3.1. Reliable activation of RGC spiking by low-amplitude sinusoidal stimuli

The recording presented in figure 1(D) suggests that application of sinusoidal stimuli leads to reliable RGC spiking. In the following, we test the hypothesis of reliable spiking for stimulation protocols applied to rd10 retina.

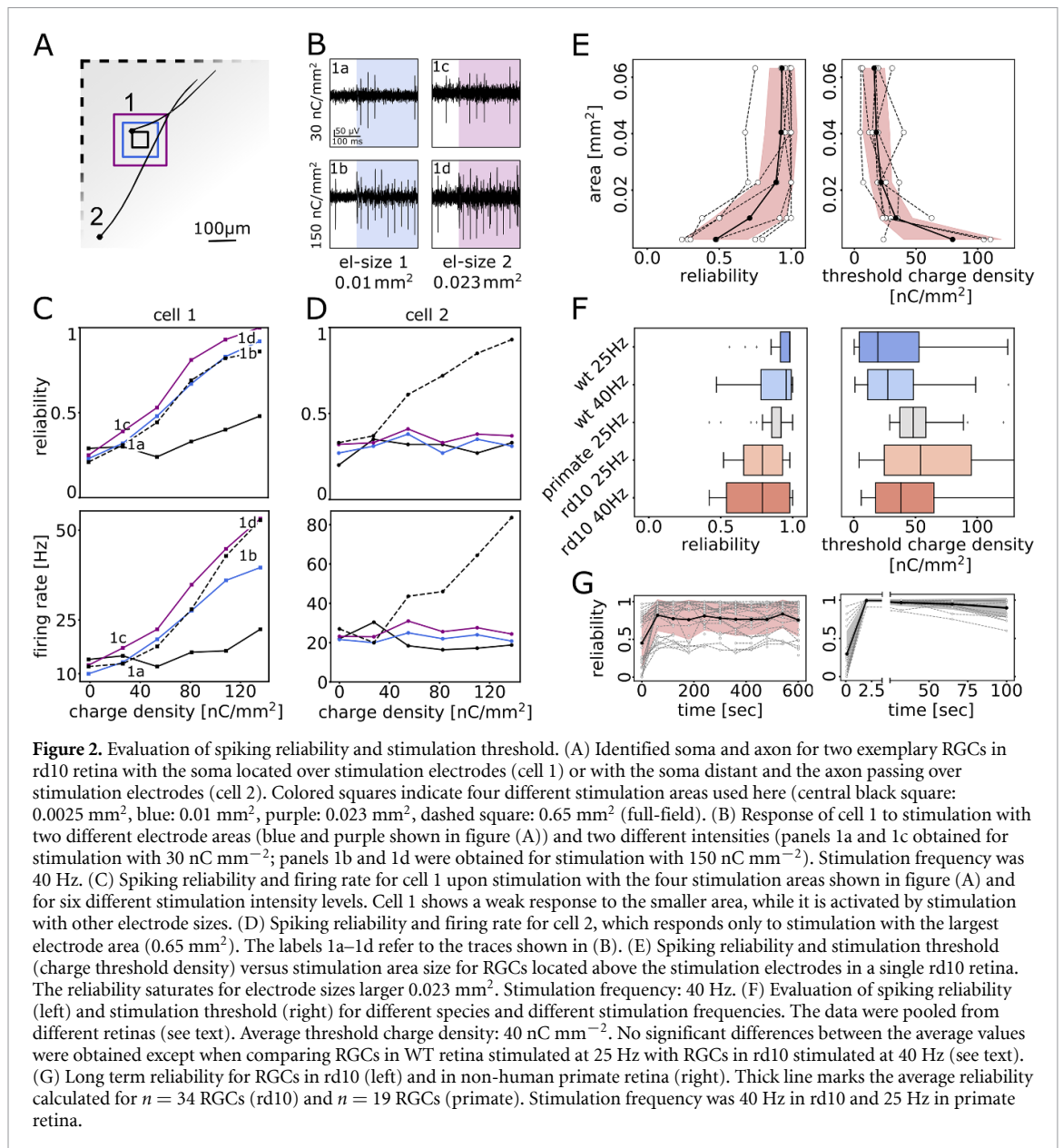
CMOS MEA recording allows us to precisely detect RGC soma and axon locations upon STA of multiple electrical images [34, 35] (figure 1(A), for details see the section 2). We recorded and analyzed in the same retina two prototypical cases: an RGC above the center of the stimulation electrode (figure 2(A), cell 1) and an RGC outside the electrode but with its axon crossing the electrodes (figure 2(A), cell 2). In figures 2(B)–(D) we show the evoked activity for these two exemplary cells upon stimulation with increasing electrode areas. To enable a better comparison to previous studies we calculated an equivalent electrode diameter: 56.7 μm , 113.5 μm and 170 μm (figure 2(A)). The normalized reliability parameter quantifies if at least one spike is evoked per stimulation phase (see description in section 2). For cell 1, located above the stimulation electrodes, stimulation with a small electrode area (equivalent diameter: 56.7 μm) proved to be ineffective up to the charge density of 150 nC mm^{-2} (equivalent to: 0.6 nC). For larger stimulation areas (0.01 mm^2 and 0.023 mm^2) we observe that stimulation with low amplitude evokes few spikes. Increasing the charge density to 150 nC mm^{-2} leads to a reliability close to 1, which corresponds to one spike detected in every stimulus phase (figures 2(B) and (C)). For cell 2, with the soma located far away and the axon passing over the stimulation electrodes, there is no effect for

localized stimulation. To confirm the general excitability of this RGC we demonstrate activation using a large electrode (0.65 mm^2) covering the RGC and its presynaptic circuit. For these two cells we also calculated the stimulus-induced firing rate. The firing rate is used to determine the threshold charge density, defined as the increase of the spontaneous activity by 30% (figure 2(D)).

From the example cells shown in figure 2(A) we proceed to the entire RGC population ($n = 102$) identified in this retina and select RGCs located directly over the stimulation electrodes ($n = 6$). For these RGCs cells we calculated reliability and threshold charge density for different stimulation areas (figure 2(E)). The reliability and the threshold charge density approaches a narrow range (r : 0.8–1, threshold: 10–30 nC mm^{-2} , equivalent to 0.2–0.6 nC) for electrodes larger than 0.02 mm^2 .

Retina degeneration causes a remodeling of the inner retina network in the mice blind model rd10, compared to the healthy retina in WT. It is not clear yet to which degree this modification affects the response to electrical stimulation [36]. Moreover, for clinical applications, it is very valuable to evaluate if results obtained in rodent retina are confirmed in other models, such as non-human primate. We therefore evaluated stimulation thresholds and response reliability for healthy mouse ($n = 47$ RGCs at 25 Hz; $n = 43$ at 40 Hz identified in three retinas, C57Bl6/J), non-human primate retina ($n = 36$ RGCs identified in two retinas) and RGCs in adult rd10 ($n = 77/76$ RGCs at 25/40 Hz RGCs, $n = 2$ retinas) for two different stimulation frequency (figure 2(F)). No statistical difference (Mann–Whitney U -test) was found among the different conditions except when comparing RGCs in WT retina stimulated at 25 Hz with RGCs in rd10 (40 Hz). Here the p -values for average reliability and threshold were 0.026 and 0.013, respectively. In summary, the low stimulation threshold and high reliability appears to translate between different species.

Finally, reliable activation over extended time intervals is crucial for application of a stimulation strategy in an implant. We continuously stimulated retina tissue and recorded activity at specific time points to evaluate reliability in rd10 and in primate retina. Ganglion cells ($n = 34$) in rd10 retina showed high spiking reliability without spiking dropouts for a stimulation charge density of 150 nC mm^{-2} . Similar results were found in primate retina ($n = 19$; 25 Hz, figure 2(G)). Reliable RGC activation has been challenging for certain pulse durations (1 and 2 ms) in the healthy retina [4, 37]. Failure of reliable activation might be one reason for the fading of visual percepts reported for blind patients [5, 38]. Control experiments stimulating RGCs in rd10 retina support the finding that pulsatile waveforms similar to those used in retinal implants (1 and 2 ms pulse duration) fail to reliably stimulate retinal circuits



of photoreceptor-degenerated retina (supplementary figure 2). In summary, the results presented here confirm our first hypothesis of reliable modulation of the retinal networks and cells located above the stimulation electrodes by sinusoidal stimuli.

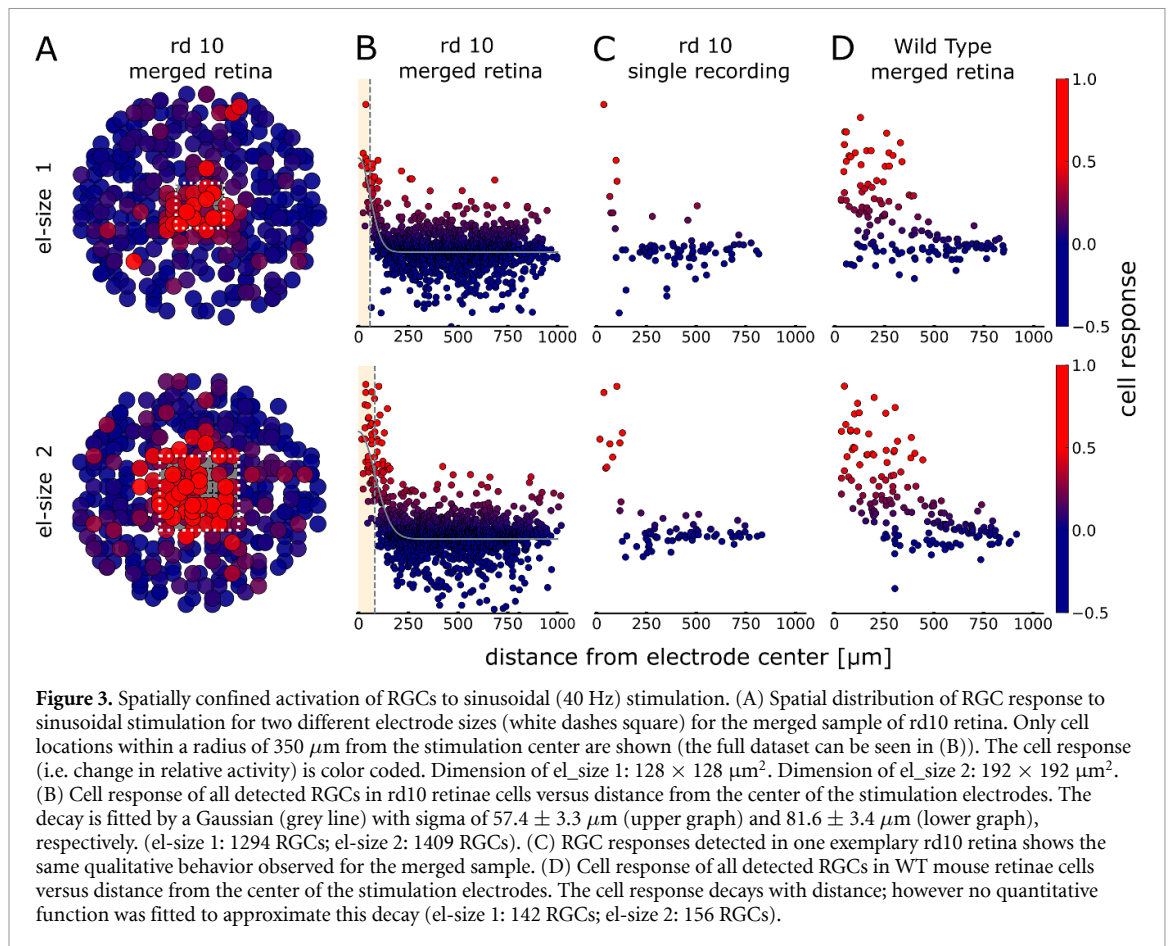
3.2. Spatially confined modulation of retinal networks and stimulation mechanism

Based on the results presented in figure 2, two stimulation strategies may be pursued: (a) stimulation at the stimulation threshold (~ 40 nC mm⁻²) or (b) stimulation using that amplitude (150 nC mm⁻²) which leads to very high spiking reliability. We favored the second strategy here, as this ensures that fast changes in stimulation amplitude are immediately translated in modulation of the firing rate while staying in the range for safe stimulation. For this stimulation amplitude we evaluated the spatial selectivity

of stimulation of RGC activity (figure 3(A)) for two different stimulation electrodes areas: 0.01 mm² and 0.023 mm² (figure 2(A): blue and purple electrode, el-size 1 and 2). In the following we evaluated recordings upon a stimulation frequency of 40 Hz only, as this frequency is considered sufficiently high to provide a continuous percept [39].

The high spontaneous activity encountered in photoreceptor-degenerated retinas (rd10) makes it difficult to use the reliability index and absolute firing rate to measure spatial selectivity over the total RGC population. Instead, we evaluated the stimulated RGC response, defined as a change in firing rate normalized to the spontaneous activity (see section 2 for definition of cell response).

In order to estimate the spatial selectivity of sinusoidal stimulation we evaluated the relative activation for a large population of RGCs. Even with



CMOS-MEAs the identification of RGCs within 1 mm^2 is limited to hundreds of cells/retina, which underestimates the true number of RGCs within this area. We therefore pooled different recordings and aligned them to the center of the stimulation area. We thereby reached a cell density of about $1000 \text{ cells mm}^{-2}$ in rd10 retina (figures 3(A) and (B) and dataset used in figures 4 and 5) based on recordings from different retinal. The cell density is within the range of RGC density reported in the healthy mouse [40]. From now on, we will refer to these artificial samples as ‘merged retina’. Some experiments were performed at different positions of the same retina. In this case, to be certain that stimulation was affecting a different subset of RGCs, sufficiently large distances were maintained between the different stimulation area centers.

The spatial selectivity of sinusoidal stimulation for the ‘merged rd10 retina’ is shown in figure 3(B). Cell response decreases rapidly outside the stimulation area (marked by white dashed line). We estimated the radius of activation around the stimulus center as the sigma of a Gaussian fit to the cell’s response. For the two electrode sizes investigated here the calculated activation radii were $57.4 \pm 3.3 \mu\text{m}$ and $81.6 \pm 3.4 \mu\text{m}$, respectively. These values are close to the electrode/object size (equivalent radius: $56.7 \mu\text{m}$ and $85 \mu\text{m}$). The spatial selectivity

is also found in individual retinal (figure 3(C)), although the estimation of the radius of activation was not possible because of the reduced number of cells.

To further investigate spatial selectivity and the stimulation mechanism we repeated the same analysis on WT retina (figure 3(D)). Our results show a substantial difference of RGC activation in WT retina as compared to rd10. The activation of RGCs outside the electrode area indicates the recruitment of the RGC network not identified in rd10 retina. Therefore, in WT retina, stimulation may involve the retinal network presynaptic to the RGC. To prove this hypothesis, we applied ionotropic glutamate receptor blockers (DNQX + AP5), which block the excitatory input to the RGCs. The results obtained for WT retina after drug application resembled the results in rd10 with a radius of activation of $73.2 \pm 10.9 \mu\text{m}$. There was no difference in RGC activation in rd10 retina before and after drug application (75.4 ± 6.6 and $80.5 \pm 5.8 \mu\text{m}$, respectively) as shown in the supplementary figure 3.

The stimulation results for the ‘merged rd10 retina’ (figure 3) comprise more than a thousand cells (el-size 1: 0.01 mm^2 , corresponding RGC density: 1294 mm^{-2} ; el-size 2: 0.023 mm^2 ; corresponding density: 1409 mm^{-2}). Out of these RGCs, only a few cells distant from the stimulation electrodes

Table 1. Results of spatial discrimination for different electrode size (area) and spatial jitters. Δx = distance between Gaussian fit centers of stimulus 1 and 2. $\sigma_1, \sigma_2 = \sigma$ of Gaussian fit for stimulus 1 and 2. Accuracy = discrimination accuracy between stimulus 1 and 2 calculated with the LR model for the merged sample (merged) and the mean (mean), the worst (min) and best (max) accuracy for single recording. The results obtained for the five experimental conditions are visualized in figure 4(B). The reported discrimination accuracy is visualized in figure 4(C).

Area (mm ²) / jitter (μ m)	Δx	σ_1	σ_2	Accuracy (merged)	Accuracy (mean)	Accuracy (min)	Accuracy (max)
0.01/32	29.8 \pm 5.9	53.9 \pm 3.2	52.7 \pm 3.2	0.62	0.66	0.55	0.83
0.01/64	59.2 \pm 6.0	55.7 \pm 3.1	62.2 \pm 3.1	0.7	0.73	0.6	0.83
0.023/32	18.7 \pm 5.6	76.6 \pm 2.9	70.6 \pm 2.9	0.9	0.69	0.59	0.86
0.023/64	50.3 \pm 6.4	77.2 \pm 3.3	77.2 \pm 3.3	1	0.87	0.73	0.99
0.023/128	120.4 \pm 4.7	76.3 \pm 2.6	79.1 \pm 2.6	1	0.99	0.97	1

showed an increase in activity. To investigate if these cells may be activated through axonal stimulation we selected those cells with their axon passing over the stimulation electrodes. Electrical imaging of the axon path using the CMOS MEA allowed us to identify all RGCs with axons passing over the stimulation electrodes (el-size 1: $n = 83$, el-size 2, $n = 74$; supplementary figure 5). We could not detect a significant change of firing rate (stimulus charge density: 150 nC mm⁻²) in any of these RGCs and thus conclude that sinusoidal stimulation activates RGCs in photoreceptor-degenerated retina within a very confined area.

Our results suggest two different stimulation mechanisms. The presence of the functional retinal network in WT retinæ (mouse and primate) was tested by simple flicker stimuli (1 Hz) and the recording of light-induced RGC activity [26, 41]. In WT retinæ sinusoidal stimuli activate the retinal network, reflected by a spatially extended activation range (figure 3(D) and supplementary figure 3), which becomes more localized after the addition of synaptic blockers (supplementary figure 3). This result is in line with a previous report [15]. In rd10 retina we recorded the previously reported local field potentials (LFPs) [42, 43], which reflect the aberrant activity of retinal interneurons [44] (supplementary figure 4). After application of glutamate receptor blockers, the LFPs disappeared, in agreement with previous reports, and reflecting the activity of the retinal interneuron network. However, the RGC spiking pattern in rd10 retinæ stimulated by sinusoidal stimuli was not influenced by the presence of the blockers (supplementary figures 3 and 4), indicating direct RGC activation. An indication that the inner retinal network in rd10 retina can be activated is demonstrated by the RGC activation upon square-wave pulses (2 ms, supplementary figure 2). Stimulus-induced RGC spikes were identified in a time interval 4–20 ms after stimulus onset. Further work is required to conclusively elucidate the unexpected result of direct RGC activation detected upon sinusoidal stimulation in rd10 retina.

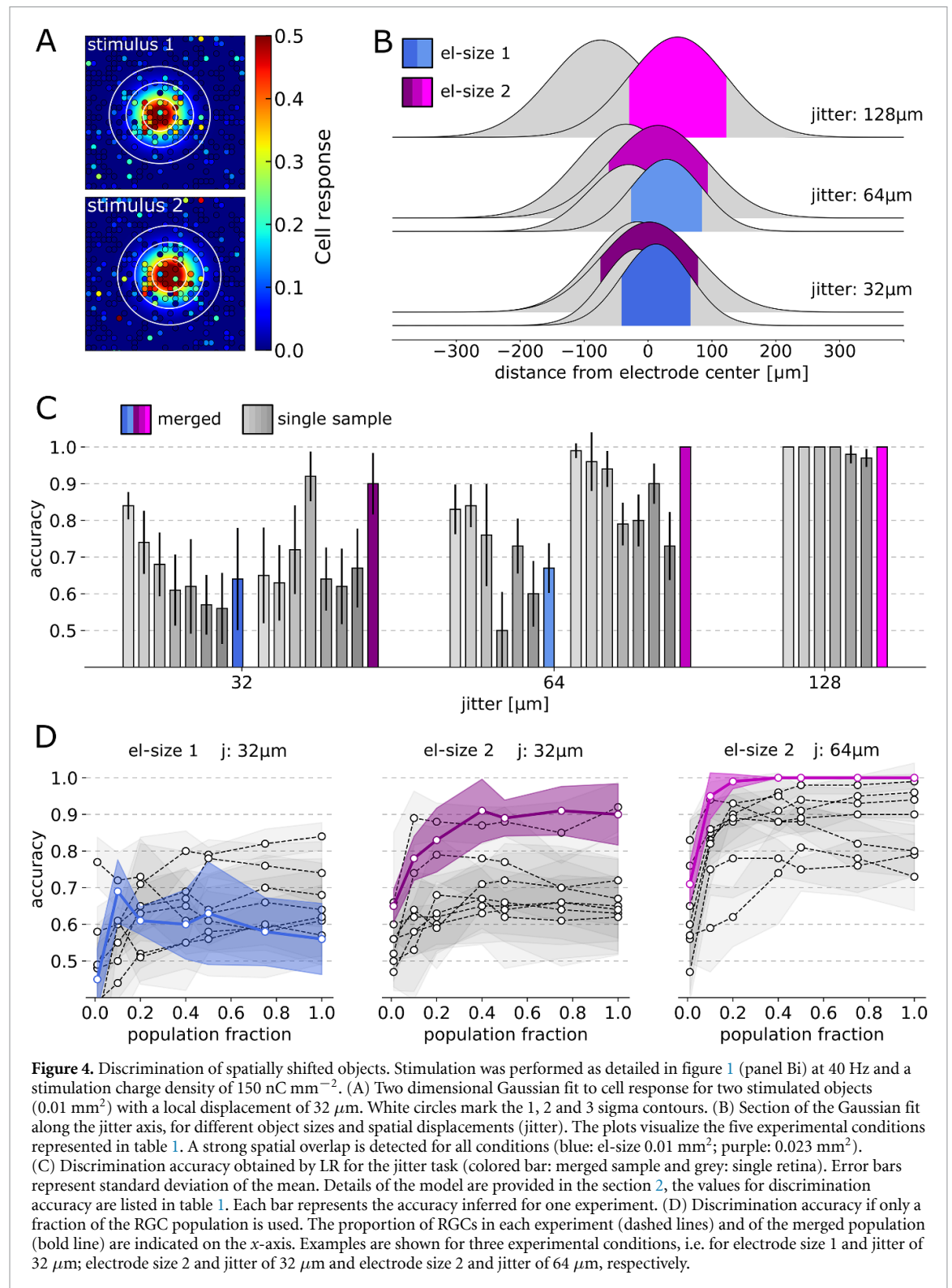
3.3. Discrimination of spatially displaced objects

Once we established the spatial selectivity of sinusoidal stimulation we proceeded to test how

this translates into encoding of spatial information. It has been reported in clinical trials, that retina implants failed to encode small shapes [7, 45]. We therefore opted for a protocol to investigate discrimination of distinct response patterns with very localized stimuli. We performed the spatial displacement protocol described in figure 1(B), (details in section 2). We selected two subsets of stimulation electrodes, each forming two equal shapes, displaced by a defined spatial jitter. Alternating the two stimuli for 50 repetitions, we tested the ability to discriminate the two stimuli based on the RGC population response. We used this protocol to test two sizes of stimulation areas, 0.01 mm² and 0.023 mm², and different displacements, 32 μ m and 64 μ m displacements for the 1st area and 32, 64, and 128 μ m for the 2nd area.

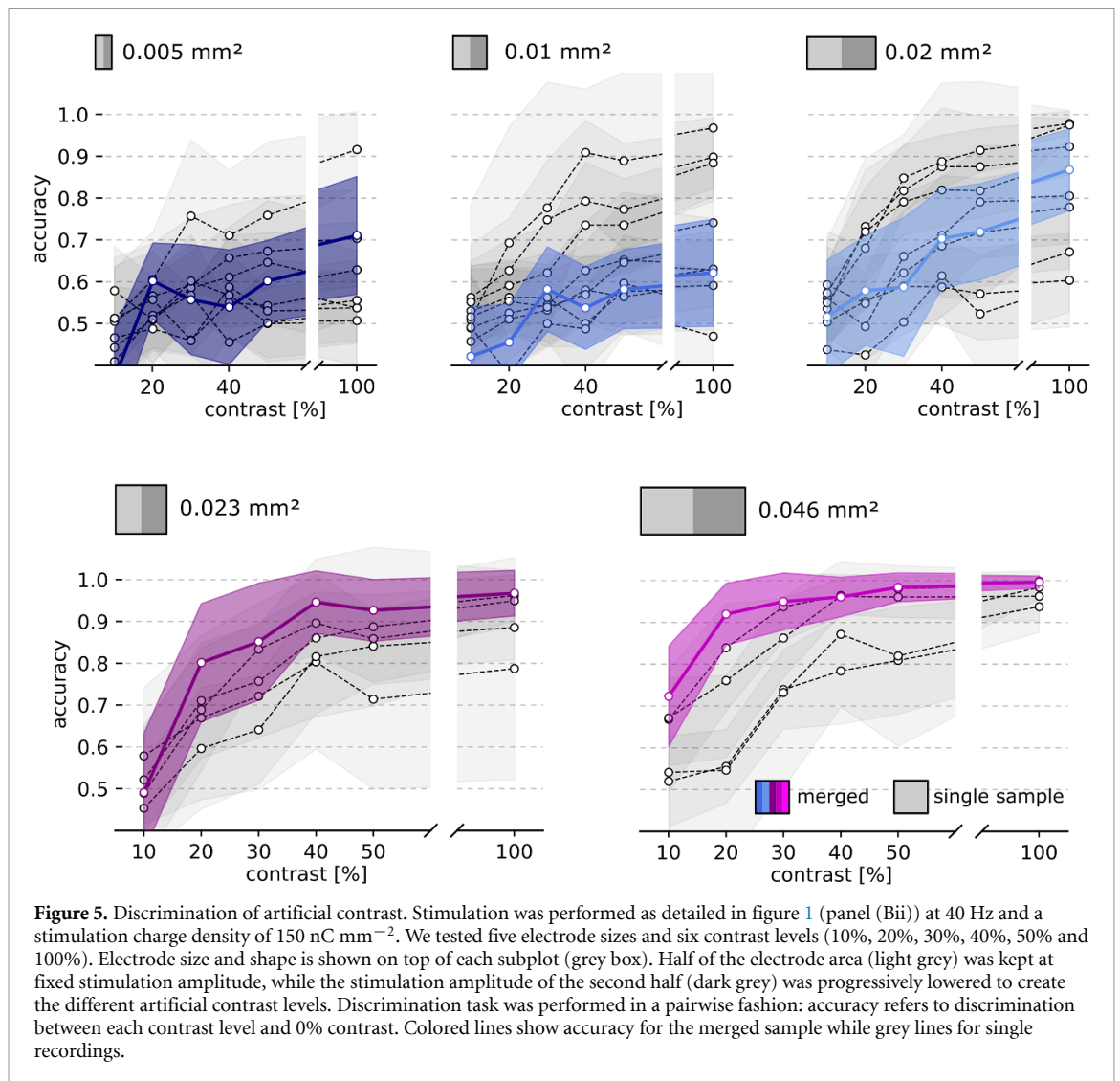
We evaluated the accuracy of discriminating the response to the two stimuli, first fitting the response with a two-dimensional symmetrical Gaussian distribution (figure 4(A)). A summary of the Gaussian fit parameters, i.e. estimated distance (Δx) from distribution center along jitter axis and sigma for the two Gaussian fits is shown in table 1. Data presented in table 1 are visualized in figure 4(B), where a one-dimensional representation of these Gaussian distributions along the axis of spatial displacement is shown. The Gaussian distributions of cell responses strongly overlap for all the stimulation protocols. Thus, assuming a model which considers a population of RGC independent responses cannot accurately discriminate between the two stimulus conditions. Therefore we investigated if an optimal linear decoder (LR model) [46] may correctly discriminate the presented stimuli.

In this model, we treat the two stimuli as binary events i.e. 0 for the 1st stimulus and 1 for the 2nd stimulus. We train the model to predict the probability of each event (or stimulus identity), given the responses of the RGC population. We then compute the accuracy of the model predictions on a test dataset that was not shown to the model during training (see section 2 for details). Results for test sets are shown in figure 4(B) and table 1. For the 64 μ m jitter, we were able to discriminate with high accuracy for both electrode sizes. El-size 1 (0.01 mm²):



0.7/0.73 (merged/mean of single retinas) and el-size 2 (0.023 mm^2): 1/0.87. For the smaller jitter, $32 \mu\text{m}$, only stimulation with the larger size provided good results: 0.9/0.69. The LR parameter for each cell correlated well with the difference in firing rates between the two stimulus conditions (supplementary figure 6). Low prediction accuracy obtained for small objects (small electrode area) can be explained by the reduced number of cells affected by the stimulation.

The discrimination performance was highly variable across different retina samples. The best sample had a test accuracy of over 0.8 for all stimulation areas and jitter conditions. However, there were samples that had very poor performance for smaller stimulation areas, and smaller jitters. Since we record a finite number of cells, we posit that in some of the retina samples we may have missed those cells which would best predict the stimulus identity.



Finally, we investigate how the number of neurons affected the prediction accuracy. We calculated the accuracy for different subsets of the population, selecting the fraction of neurons with the highest LR parameter values. For most samples, we found that only 20%–40% of the neurons with highest parameter values were needed in order to reach the accuracy of the full population (figure 4(D)). This effect was consistent across all protocols and samples. The LR weights are positively correlated with the difference in firing rate between the two stimulus conditions (supplementary figure 4), while the cell response is in turn negatively correlated with the cell's distance from the stimulation electrodes (see figures 3(B) and (C)). This indicates that the fraction of the neural population located closest to stimulating electrodes is the most predictive of the stimulus identity.

3.3.1. Discrimination of artificial contrast

We performed a similar experiment and analysis as shown in figure 4 and determined the discrimination accuracy for stimuli with different artificial contrast. Details of the stimulation protocol are provided

in the section 2. Briefly, we tested five object sizes (0.005–0.046 mm²) and seven contrast levels. We tested the discrimination accuracy in a pairwise fashion, comparing the cell response of homogenous objects (0% contrast) to stimulated objects with the remaining six contrast levels. Evaluation using the LR model reveals the following results, presented in figure 5: (a) discrimination accuracy increases with contrast and reaches (in most conditions) a plateau at 40%–50% contrast; (b) discrimination accuracy improves with object size. And once again, the discrimination accuracy varies considerably across different retinal samples. The best discrimination performance at the lowest contrast tested (10%) was obtained for the largest object size with 80% accuracy. This result translates to a discrimination of total stimulation charge of 0.5 nC for electrode sizes of 0.023 mm².

4. Discussion

In this study, we demonstrated that sinusoidal continuous stimulation enables robust and spatially

selective activation of RGCs. Our approach, performed in epiretinal configuration, avoids axonal stimulation and enables discrimination of electrically stimulated objects displaced by as little as $32\ \mu\text{m}$ (1° visual angle).

4.1. High-density MEAs enable continuous bidirectional interfacing

Before discussing the obstacles of artificial stimulation which were overcome by sinusoidal stimulation, we briefly highlight the enabling technology. Simultaneous electrical stimulation and recording of neuronal activity is a challenging task due to the so-called stimulation artefact. A solution of this problem is offered by high-density MEAs, with electrode distances in the order of $\sim 10\text{--}20\ \mu\text{m}$ [22, 47]. Using CMOS-based high density MEAs [35], electrical imaging of stimulated axonal activity in neuronal cell cultures using short stimulus pulses ($<100\ \mu\text{s}$) was reported [35]. Electrical stimulation with single electrodes followed by electrophysiological imaging of axonal activation has been reported for *ex vivo* primate retina [14, 16], but was restricted to short stimuli ($<100\ \mu\text{s}$) and larger electrode separations ($60\ \mu\text{m}$). The CMOS-based MEA presented here, employs two separate but intermingled electrode arrays, one for stimulation and one for recording (figure 1(B)). It enables the selection of arbitrary stimulation areas and the application of arbitrary stimulus waveforms [18] together with electrical imaging of cell and axon positions, eventually leading to a truly bidirectional electrical interfacing.

4.2. Obstacles overcome in artificial stimulation

The presented sinusoidal stimulation approach overcomes the following obstacles in artificial stimulation. First, we were able to avoid fading or desensitization of the evoked ganglion activity as reported previously for certain pulsatile stimuli [4, 48]; but see [12, 49], despite using a stimulation frequency (40 Hz) which is well above the flicker fusion frequency for the mouse retina. Reduced desensitization of RGC spiking to sinusoidal stimuli has been reported in healthy rat [50] or rabbit RGCs [51], which is in line with our results presented for RGCs in rd10 retina.

Second, we used very low current amplitudes ($0.2\text{--}0.4\ \mu\text{A}$) to activate RGCs. The threshold charge density of $40\ \text{nC mm}^{-2}$ (figures 2(E) and (F)) is about 20 times smaller than previously reported for epiretinal pulsatile stimuli (reviewed by [52]) using electrodes of similar size ($0.01\ \text{mm}^2$) and about ten times smaller than charge densities evaluated for subretinal millisecond-long pulsatile stimuli (reviewed in [23]) and far below electrode or tissue damage thresholds. The total stimulation charge of $\sim 1\ \text{nC}$ required to reliably activate RGCs is, however, in the same range of previously reported values for pulsatile millisecond-long stimuli [53, 54]. This

indicates that RGCs are capable of integrating the stimulation current over several milliseconds.

Third, the spatial activation of RGCs was confined to the stimulation electrodes avoiding the problem of axonal stimulation in epiretinal configuration [14, 55, 56]. This result (figure 2(A), supplementary figure 5) is in line with a recent study using smooth wave stimuli [18] but appears to contradict previous studies, where action potential initiation at the edge of the epiretinal stimulation electrode was demonstrated [56]. However, for long stimulus durations ($>10\ \text{ms}$) the RGC stimulation mechanism may not be dominated by the sodium channels in the axon (Fried *et al* 2009) or by the ‘activating function’ [57] but by the depolarization of the cell soma in an homogenous electric field, as suggested by [58]. The avoidance of axonal stimulation using long pulses (either square-wave or sinusoidal) has indeed been suggested by calcium imaging of RGC activity [20]; however that technique does not allow resolution of individual axonal action potentials. Several other axon-avoidance strategies have been either simulated [59, 60] or have been tested experimentally by other groups [16, 61, 62].

4.3. Performance and limitations in discriminating spatial and contrast information

We compare our results of spatial and contrast discrimination (figures 4 and 5) to previous work. Spatial resolution based on grating stimuli has been estimated for subretinal stimulation of photoreceptor-degenerated rat retina to $48\ \mu\text{m}$ [63], a value limited by the resolution of the stimulation array used there. The estimate was based on cortical visually evoked potentials, which does not allow to infer the underlying retinal activity. A similar accuracy ($30\text{--}60\ \mu\text{m}$) has been inferred in primate retina for epiretinal stimulation using short pulses [16]. The discrimination of $32\ \mu\text{m}$ spatial shift of overlapping objects obtained here (figure 4) would correspond in an human eye to a spatial resolution of $20/130$, i.e. above legal blindness. Future *in vivo* studies need to confirm this high resolution. For large objects (6°) a contrast discrimination of 10% could be achieved here at an accuracy of 80%. This value is superior to previous reports in blind rats [17] and in humans [5] and in the same range as inferred from the spike-time pattern of stimulated single RGC activity [64].

The high discrimination obtained here relies on LR, a model which emphasized those cells, which change their response upon stimulation. Recent neurophysiological reports show that a few simultaneously active RGCs modulate one postsynaptic neurons [65, 66], in line with a neurobiological implementation of LR. Remarkably, the discrimination accuracy varied considerably among experiments, even comprising different retinal portions from the same eye. Recently, it has been noted that the retinal degeneration reduces the consistency of

RGC responses [67]. However, that effect was mediated by network activation; whereas here we demonstrate a direct activation of RGCs in rd10. If this finding translates to the human retina, the reorganization of the presynaptic network [68] may play a minor role for epiretinal artificial stimulation. The discrimination performance of object position or object contrast was higher for large objects than for small objects. We assign this result to the low number of activated cells for small stimulus shapes. However, a related contribution may be the weaker cell response and lower reliability (figures 2(E), 3(B) and supplementary figure 6) obtained for small electrodes. Future studies may investigate smaller stimulation electrodes with higher specific capacitance and thus higher stimulation charge density [69, 70]. Increasing the charge density, especially considering the low charge threshold inferred here, would likely improve spatial and contrast discrimination.

4.4. Future stimulation strategies for retinal prosthetics

Although the presented concept is encouraging, we are aware that it represents only an initial step toward achieving a more realistic visual experience. The restriction of the electric field will be important to further reduce the spatial spread of the electric field, which defines the spatial activation range and which ranged here between ~ 52 and $79\ \mu\text{m}$ (figure 3). The confinement or steering of the stimulating electrical field [11, 71] is part of ongoing research and may be combined in future with sinusoidal or smooth-wave stimuli. Such stimuli can be delivered by an implantable high-density MEA [72]. Aiming for cell-type specific stimulation is a second future goal, which has not been reported for low-frequency sinusoidal stimulation. However, a recent simulation study suggests smooth waveforms to selectively activate ON or OFF bipolar cells [73]. A recent experimental study [74] reports that ON RGCs are preferentially activated by half-wave sinusoidal pulses (10 ms, corresponding to a frequency of 50 Hz). Preferred activation of different RGC cell types in epiretinal configuration has been reported to various degrees using low frequency [75] and high-frequency pulses [76–78]. As an alternative to smooth waveforms, the selective activation of specific RGCs by very short pulses ($<100\ \mu\text{s}$) after identification of the cell type using a high-density MEA has been reported recently [16]. Future work needs to identify, to which degree the ON and OFF dichotomy remains valid in photoreceptor-degenerated retinæ and which stimuli are most efficient to selectively stimulate one cell class versus another.

5. Conclusion

With the presented sinusoidal approach, we discriminated with high accuracy overlapping objects

(defined by stimulating electrodes) or small contrast values (defined by stimulation strength) using the RGC activity recorded in photoreceptor-degenerated rd10 mouse retina. In epiretinal configuration we first demonstrated that sinusoidal stimulation evokes reliable and spatially confined activity in RGCs located above the stimulation electrode. Crucial for this study was stimulation of multiple objects of variable size combined with simultaneous recording of the evoked activity—an approach well-suited for the investigation of further neuroprosthetic applications. While the sinusoidal approach overcomes several obstacles of retinal prosthetics for the specific stimulation of certain cell classes (i.e. ON or OFF RGCs) other stimulus waveforms need to be investigated.

Data availability statement

The data that support the findings of this study are available upon reasonable request from the authors.

Acknowledgments

This work was supported by the German Research Foundation (DFG, SFB 1233 ‘Robust Vision’, Project Number 2766935), by the German Federal Ministry of Education and Research (FKZ 161L0059A) and by Germany’s Excellence Strategy (EXC-Number 2064/1, Project Number 390727645). The authors acknowledge TU Wien Bibliothek for financial support through its Open Access Funding Program. The authors thank Dr. Paul Werginz for helpful discussion on the manuscript.

ORCID iDs

Andrea Corna  <https://orcid.org/0000-0002-3209-6719>

Jakob H Macke  <https://orcid.org/0000-0001-5154-8912>

Günther Zeck  <https://orcid.org/0000-0003-3998-9883>

References

- [1] Edwards T L, Cotttriall C L, Xue K, Simunovic M P, Ramsden J D, Zrenner E and MacLaren R E 2018 Assessment of the electronic retinal implant alpha AMS in restoring vision to blind patients with end-stage retinitis pigmentosa *Ophthalmology* **125** 432–43
- [2] Zrenner E et al 2011 Subretinal electronic chips allow blind patients to read letters and combine them to words *Proc. Biol. Sci.* **278** 1489–97
- [3] Palanker D V, Le Mer Y, Mohand-Said S, Hornig R, Buc G, Deterre M and Sahel J A 2020 Photovoltaic restoration of central vision in atrophic age-related macular degeneration *Ophthalmology* **127** 1097–104
- [4] Jensen R J and Rizzo J F 3rd 2007 Responses of ganglion cells to repetitive electrical stimulation of the retina *J. Neural. Eng.* **4** S1–6

- [5] Stingl K *et al* 2015 Subretinal visual implant alpha IMS—clinical trial interim report *Vis. Res.* **111** 149–60
- [6] Goetz G A and Palanker D V 2016 Electronic approaches to restoration of sight *Rep. Prog. Phys. Phys. Soc.* **79** 096701
- [7] Stingl K *et al* 2017 Interim results of a multicenter trial with the new electronic subretinal implant alpha AMS in 15 patients blind from inherited retinal degenerations *Front. Neurosci.* **11** 445
- [8] Flores T, Huang T, Bhuckory M, Ho E, Chen Z, Dalal R, Galambos L, Kamins T, Mathieson K and Palanker D 2019 Honeycomb-shaped electro-neural interface enables cellular-scale pixels in subretinal prosthesis *Sci. Rep.* **9** 10657
- [9] Spencer T C, Fallon J B, Thien P C and Shivdasani M N 2016 Spatial restriction of neural activation using focused multipolar stimulation with a retinal prosthesis *Invest. Ophthalmol. Vis. Sci.* **57** 3181–91
- [10] Flores T, Lei X, Huang T, Lorach H, Dalal R, Galambos L, Kamins T, Mathieson K and Palanker D 2018 Optimization of pillar electrodes in subretinal prosthesis for enhanced proximity to target neurons *J. Neural. Eng.* **15** 036011
- [11] Matteucci P B, Chen S C, Tsai D, Dodds C W, Dokos S, Morley J W, Lovell N H and Suaning G J 2013 Current steering in retinal stimulation via a quasimonopolar stimulation paradigm *Invest. Ophthalmol. Vis. Sci.* **54** 4307–20
- [12] Fried S I, Hsueh H A and Werblin F S 2006 A method for generating precise temporal patterns of retinal spiking using prosthetic stimulation *J. Neurophysiol.* **95** 970–8
- [13] Sekirnjak C, Hottowy P, Sher A, Dabrowski W, Litke A M and Chichilnisky E J 2008 High-resolution electrical stimulation of primate retina for epiretinal implant design *J. Neurosci.* **28** 4446–56
- [14] Grosberg L E *et al* 2017 Activation of ganglion cells and axon bundles using epiretinal electrical stimulation *J. Neurophysiol.* **118** 1457–71
- [15] Freeman D K, Eddington D K, Rizzo J F 3rd and Fried S I 2010 Selective activation of neuronal targets with sinusoidal electric stimulation *J. Neurophysiol.* **104** 2778–91
- [16] Fan V H, Grosberg L E, Madugula S S, Hottowy P, Dabrowski W, Sher A, Litke A M and Chichilnisky E J 2019 Epiretinal stimulation with local returns enhances selectivity at cellular resolution *J. Neural. Eng.* **16** 025001
- [17] Lorach H *et al* 2015 Photovoltaic restoration of sight with high visual acuity *Nat. Med.* **21** 476–82
- [18] Hoffling L, Oesterle J, Berens P and Zeck G 2020 Probing and predicting ganglion cell responses to smooth electrical stimulation in healthy and blind mouse retina *Sci. Rep.* **10** 5248
- [19] Rathbun D L, Ghorbani N, Shabani H, Zrenner E and Hosseinzadeh Z 2018 Spike-triggered average electrical stimuli as input filters for bionic vision—a perspective *J. Neural. Eng.* **15** 063002
- [20] Weitz A C, Nanduri D, Behrend M R, Gonzalez-Calle A, Greenberg R J, Humayun M S, Chow R H and Weiland J D 2015 Improving the spatial resolution of epiretinal implants by increasing stimulus pulse duration *Sci. Transl. Med.* **7** 318ra203
- [21] Ho E, Smith R, Goetz G, Lei X, Galambos L, Kamins T I, Harris J, Mathieson K, Palanker D and Sher A 2018 Spatiotemporal characteristics of retinal response to network-mediated photovoltaic stimulation *J. Neurophysiol.* **119** 389–400
- [22] Bertotti G, Velychko D, Dodel N, Keil S, Wolansky D, Tillak B, Schreiter M, Röhrer S, Zeck G and Thewes R 2014 A CMOS-based sensor array for *in-vitro* neural tissue interfacing with 4225 recording sites and 1024 stimulation sites *Biomedical Circuits and Systems Conf. (Biocas), 2014 IEEE (IEEE)* pp 304–7
- [23] Corna A, Herrmann T and Zeck G 2018 Electrode-size dependent thresholds in subretinal neuroprosthetic stimulation *J. Neural. Eng.* **15** 045003
- [24] Gargini C, Terzibasi E, Mazzoni F and Strettoi E 2007 Retinal organization in the retinal degeneration 10 (rd10) mutant mouse: a morphological and ERG study *J. Comp. Neurol.* **500** 222–38
- [25] Leibig C, Wachtler T and Zeck G 2016 Unsupervised neural spike sorting for high-density microelectrode arrays with convolutive independent component analysis *J. Neurosci. Methods* **271** 1–13
- [26] Zeck G, Jetter F, Channappa L, Bertotti G and Thewes R 2017 Electrical imaging: investigating cellular function at high resolution *Adv. Biosyst.* **1** 1700107
- [27] Eickenscheidt M, Jenkner M, Thewes R, Fromherz P and Zeck G 2012 Electrical stimulation of retinal neurons in epiretinal and subretinal configuration using a multicapacitor array *J. Neurophysiol.* **107** 2742–55
- [28] McCullagh P and Nelder J A 1989 *Generalized Linear Models* 2nd edn (Boca Raton, FL: CRC Press) (<https://doi.org/10.1201/9780203753736>)
- [29] Virtanen P, Gommers R, Oliphant T E, Haberland M, Reddy T, Cournapeau D, Burovski E, Peterson P, Weckesser W and Bright J 2020 SciPy 1.0: fundamental algorithms for scientific computing in Python *Nat. Methods* **17** 261–72
- [30] Cessie S L and Houwelingen J C V 1992 Ridge estimators in logistic regression *J. R. Stat. Soc. Ser. C* **41** 191–201
- [31] Hierlemann A 2017 Direct interfacing of neurons to highly integrated microsystems *Micro Electro Mechanical Systems (MEMS), 2017 IEEE 30th Int. Conf. on IEEE (IEEE)* pp 199–204
- [32] Mahadevappa M, Weiland J D, Yanai D, Fine I, Greenberg R J and Humayun M S 2005 Perceptual thresholds and electrode impedance in three retinal prosthesis subjects *IEEE Trans. Neural. Syst. Rehabil. Eng.* **13** 201–6
- [33] Newbold C, Mergen S, Richardson R, Seligman P, Millard R, Cowan R and Shepherd R 2014 Impedance changes in chronically implanted and stimulated cochlear implant electrodes *Cochlear Implants Int.* **15** 191–9
- [34] Stutzki H, Leibig C, Andreadaki A, Fischer D and Zeck G 2014 Inflammatory stimulation preserves physiological properties of retinal ganglion cells after optic nerve injury *Front. Cell Neurosci.* **8** 38
- [35] Ronchi S, Fiscella M, Marchetti C, Viswam V, Muller J, Frey U and Hierlemann A 2019 Single-cell electrical stimulation using CMOS-based high-density microelectrode arrays *Front. Neurosci.* **13** 208
- [36] Cho A, Ratliff C, Sampath A and Weiland J 2016 Changes in ganglion cell physiology during retinal degeneration influence excitability by prosthetic electrodes *J. Neural. Eng.* **13** 025001
- [37] Freeman D K and Fried S I 2011 Multiple components of ganglion cell desensitization in response to prosthetic stimulation *J. Neural. Eng.* **8** 016008
- [38] Fornas A P, Sommerhalder J and Pelizzone M 2010 Dynamics of visual perception upon electrical stimulation of the retina *Invest. Ophthalmol. Vis. Sci.* **51** 3027
- [39] Eisen-Enosh A, Farah N, Burgansky-Eliash Z, Polat U and Mandel Y 2017 Evaluation of critical flicker-fusion frequency measurement methods for the investigation of visual temporal resolution *Sci. Rep.* **7** 1–9
- [40] Jeon C J, Strettoi E and Masland R H 1998 The major cell populations of the mouse retina *J. Neurosci.* **18** 8936–46
- [41] Bertotti G, Jetter F, Keil S, Dodel N, Schreiter M, Wolansky D, Boucsein C, Boven K-H, Zeck G and Thewes R 2017 Optical stimulation effects on TiO₂ sensor dielectric used in capacitively-coupled high-density CMOS microelectrode array *IEEE Electron Device Lett.* **38** 967–70
- [42] Menzler J and Zeck G 2011 Network oscillations in rod-degenerated mouse retinas *J. Neurosci.* **31** 2280–91
- [43] Menzler J, Channappa L and Zeck G 2014 Rhythmic ganglion cell activity in bleached and blind adult mouse retinas *PLoS One* **9** e106047

- [44] Trenholm S and Awatramani G B 2015 Origins of spontaneous activity in the degenerating retina *Front. Cell Neurosci.* **9** 277
- [45] da Cruz L et al 2016 Five-year safety and performance results from the argus II retinal prosthesis system clinical trial *Ophthalmology* **123** 2248–54
- [46] Schwartz G, Macke J, Amodei D, Tang H and Berry M J 2nd 2012 Low error discrimination using a correlated population code *J. Neurophysiol.* **108** 1069–88
- [47] Yuan X Y et al 2020 Versatile live-cell activity analysis platform for characterization of neuronal dynamics at single-cell and network level *Nat. Commun.* **11** 1–14
- [48] Fornos A P, Sommerhalder J, da Cruz L, Sahel J A, Mohand-Said S, Hafezi F and Pelizzone M 2012 Temporal properties of visual perception on electrical stimulation of the retina *Invest. Ophthalmol. Vis. Sci.* **53** 2720–31
- [49] Jepson L H, Hottowy P, Weiner G A, Dabrowski W, Litke A M and Chichilnisky E J 2014 High-fidelity reproduction of spatiotemporal visual signals for retinal prosthesis *Neuron* **83** 87–92
- [50] Kotsakidis R, Meffin H, Ibbotson M R and Kamenewa T 2018 *In vitro* assessment of the differences in retinal ganglion cell responses to intra- and extracellular electrical stimulation *J. Neural. Eng.* **15** 046022
- [51] Twyford P and Fried S 2016 The retinal response to sinusoidal electrical stimulation *IEEE Trans. Neural. Syst. Rehabil. Eng.* **24** 413–23
- [52] Sekirnjak C, Hottowy P, Sher A, Dabrowski W, Litke A M and Chichilnisky E J 2006 Electrical stimulation of mammalian retinal ganglion cells with multielectrode arrays *J. Neurophysiol.* **95** 3311–27
- [53] Samba R, Herrmann T and Zeck G 2015 PEDOT-CNT coated electrodes stimulate retinal neurons at low voltage amplitudes and low charge densities *J. Neural. Eng.* **12** 016014
- [54] Stett A, Barth W, Weiss S, Haemmerle H and Zrenner E 2000 Electrical multisite stimulation of the isolated chicken retina *Vis. Res.* **40** 1785–95
- [55] Beyeler M, Nanduri D, Weiland J D, Rokem A, Boynton G M and Fine I 2019 A model of ganglion axon pathways accounts for percepts elicited by retinal implants *Sci. Rep.* **9** 9199
- [56] Eickenscheidt M and Zeck G 2014 Action potentials in retinal ganglion cells are initiated at the site of maximal curvature of the extracellular potential *J. Neural. Eng.* **11** 036006
- [57] Rattay F 1999 The basic mechanism for the electrical stimulation of the nervous system *Neuroscience* **89** 335–46
- [58] Boinagrov D, Loudin J and Palanker D 2010 Strength-duration relationship for extracellular neural stimulation: numerical and analytical models *J. Neurophysiol.* **104** 2236–48
- [59] Esler T B, Kerr R R, Tahayori B, Grayden D B, Meffin H and Burkitt A N 2018 Minimizing activation of overlying axons with epiretinal stimulation: the role of fiber orientation and electrode configuration *PLoS One* **13** e0193598
- [60] Cao X, Sui X, Lyu Q, Li L and Chai X 2015 Effects of different three-dimensional electrodes on epiretinal electrical stimulation by modeling analysis *J. Neuroeng. Rehabil.* **12** 73
- [61] Chang Y C, Haji Ghaffari D, Chow R H and Weiland J D 2019 Stimulation strategies for selective activation of retinal ganglion cell soma and threshold reduction *J. Neural. Eng.* **16** 026017
- [62] Tong W, Stamp M, Apollo N V, Ganesan K, Meffin H, Prawer S, Garrett D J and Ibbotson M R 2019 Improved visual acuity using a retinal implant and an optimized stimulation strategy *J. Neural. Eng.* **17** 016018
- [63] Ho E, Lei X, Flores T, Lorach H, Huang T, Galambos L, Kamins T, Harris J, Mathieson K and Palanker D 2019 Characteristics of prosthetic vision in rats with subretinal flat and pillar electrode arrays *J. Neural. Eng.* **16** 066027
- [64] Ho E, Lorach H, Goetz G, Laszlo F, Lei X, Kamins T, Mariani J C, Sher A and Palanker D 2018 Temporal structure in spiking patterns of ganglion cells defines perceptual thresholds in rodents with subretinal prosthesis *Sci. Rep.* **8** 3145
- [65] Alonso J M, Usrey W M and Reid R C 1996 Precisely correlated firing in cells of the lateral geniculate nucleus *Nature* **383** 815–9
- [66] Rosón M R, Bauer Y, Kotkat A H, Berens P, Euler T and Busse L 2019 Mouse dLGN receives functional input from a diverse population of retinal ganglion cells with limited convergence *Neuron* **102** 462–76. e8
- [67] Yoon Y J, Lee J I, Jang Y J, An S, Kim J H, Fried S I and Im M 2020 Retinal degeneration reduces consistency of network-mediated responses arising in ganglion cells to electric stimulation *IEEE Trans. Neural. Syst. Rehabil. Eng.* **28** 1921–30
- [68] Marc R E, Jones B W, Watt C B and Strettoi E 2003 Neural remodeling in retinal degeneration *Prog. Retin. Eye Res.* **22** 607–55
- [69] Haas J, Rudolf R, Becker M, Daschner R, Drzyzga A, Burkhardt C and Stett A 2020 Sputtered iridium oxide as electrode material for subretinal stimulation *Sens. Mater.* **32** 2903–18
- [70] Weiland J D, Anderson D J and Humayun M S 2002 *In vitro* electrical properties for iridium oxide versus titanium nitride stimulating electrodes *IEEE Trans. Biomed. Eng.* **49** 1574–9
- [71] Flores T, Goetz G, Lei X and Palanker D 2016 Optimization of return electrodes in neurostimulating arrays *J. Neural. Eng.* **13** 036010
- [72] Schütz H, Steinhoff R, Moll S, Herrmann T, Zeck G and Rothermel A 2020 Pseudo-resistor based attenuator as an efficient electrode driver for sinusoidal stimulation of retinas 2020 *IEEE Int. Symp. on Circuits and Systems (ISCAS)* (IEEE) pp 1–5
- [73] Oesterle J, Behrens C, Schroder C, Hermann T, Euler T, Franke K, Smith R G, Zeck G and Berens P 2020 Bayesian inference for biophysical neuron models enables stimulus optimization for retinal neuroprosthetics *Elife* **9** e54997
- [74] Im M, Werginz P and Fried S I 2018 Electric stimulus duration alters network-mediated responses depending on retinal ganglion cell type *J. Neural. Eng.* **15** 036010
- [75] Im M and Fried S I 2016 Temporal properties of network-mediated responses to repetitive stimuli are dependent upon retinal ganglion cell type *J. Neural. Eng.* **13** 025002
- [76] Muralidharan M, Guo T R, Shivdasani M N, Tsai D, Fried S, Li L M, Dokos S, Morley J W and Lovell N H 2020 Neural activity of functionally different retinal ganglion cells can be robustly modulated by high-rate electrical pulse trains *J. Neural. Eng.* **17** 045013
- [77] Twyford P, Cai C and Fried S 2014 Differential responses to high-frequency electrical stimulation in ON and OFF retinal ganglion cells *J. Neural. Eng.* **11** 025001
- [78] Guo T, Yang C Y, Tsai D, Muralidharan M, Suening G J, Morley J W, Dokos S and Lovell N H 2018 Closed-loop efficient searching of optimal electrical stimulation parameters for preferential excitation of retinal ganglion cells *Front. Neurosci.* **12** 168